

5 mL of trifluoroacetic acid containing 35–45 mg of 4-borono-L-phenylalanine. Next, trifluoroacetic acid was removed by passing N<sub>2</sub> under reduced pressure at a flow rate of 250 mL/min. The residue was dissolved in 4 mL of water containing 0.1 % acetic acid, and the solution was applied to a high performance liquid chromatography column, YMC-Pack ODS-A S-5 (20-mm inner diameter × 150-mm length, YMC, Kyoto, Japan), with mobile phase, water for injection containing 0.1 % acetic acid; flow rate, 10 mL/min; ultra violet detector; and radioactivity detector. The <sup>18</sup>F-FBPA fraction (retention time = 18–20 min) was corrected by adding 25 % ascorbic acid injection and 10 % sodium chloride injection. The specific activity was 20–34 GBq/mmol at the injection time and the radiochemical purity was >98 %.

### Human PET studies

Clinical studies were approved by the Ethics Committee of the Tokyo Metropolitan Institute of Gerontology. Written informed consent was obtained from each subject after the procedures were completely explained.

The whole-body distribution studies of <sup>11</sup>C-CHIBA-1001 and <sup>11</sup>C-4DST have been previously reported [6, 7]. Including <sup>11</sup>C-CHIBA-1001 and <sup>11</sup>C-4DST evaluations, a total of 18 subjects (three subjects for each radiotracer) participated in the study. Two patients (age: 45 and 54 years) in the <sup>18</sup>F-FBPA study had brain tumors, whereas, the other 16 were healthy volunteers (age 21–29 years; mean 24 ± 3 years). Whole-body PET scans were performed using SET-2400 W (Shimadzu, Kyoto, Japan) in the two-dimensional mode as described previously [6, 7]. The axial field of view was 20 cm [16]. Before injecting each radiotracer, the subjects were asked to void their bladders. Whole-body emission scans were obtained with 6–7 frames (120–130 min in total) for 1 min after administering an intravenous bolus injection of the radiotracers (500 MBq for <sup>11</sup>C radiotracers and 300 MBq for <sup>18</sup>F-FBPA). Each frame covered the body from the head to the urinary bladder, and consisted of five bed positions. In case of the first subject in the <sup>11</sup>C-CHIBA-1001 study, a unified frame duration (240 s/bed position) was used for investigating image quality and ensuring adequate frame settings [6]. For all other subjects, the duration of scanning at each bed position was increased to compensate for the short half-life of <sup>11</sup>C, i.e., 120 s/bed position for 1–3 frames, 240 s/bed position for 4–6 frames, and 360 s/bed position for the last frame. At the last frame, transmission data using a rotating <sup>68</sup>Ge/<sup>68</sup>Ga line source to correct for attenuation were acquired simultaneously [17]. The sum of the intervals for the moving bed was ~90 s/frame. Ordered-subset expectation maximization followed by application of a 6-mm FWHM Gaussian post-filter was

used to reconstruct the images. The resulting images were 128 × 128 × 25 voxels for each bed position (voxel size 4 × 4 × 6.25 mm).

Regions of interest (ROIs) were placed over organs that could be identified from the whole-body images acquired. The source organs used for dosimetry calculation were different for each radiotracer because of their respective pharmacokinetics. The ROI for red marrow was drawn on a portion of the lumbar spine, and a reference 70-kg adult male phantom was used to define the volume which was adjusted proportionally on the basis of the body weight of each subject. The decay-uncorrected time–activity course of the organs was calculated as the percentage of the injected dose per mL (%ID/mL). The number of disintegrations, formerly referred to as residence time [18], for all source organs was equal to the area under the time–activity curve multiplied by the volume of the organ ROI. The area under the time–activity curve was calculated by summing the area from time 0 to the endpoint of the scan and the area from the endpoint of the scan to infinity. The former area was calculated by trapezoidal integration. The latter area was calculated by integration of a mono-exponential curve passing through the final two scan points. For organs that were measured in two split images of different bed positions, the areas under the time–activity curve were calculated separately, and the number of disintegrations were combined into one source organ. For <sup>18</sup>F-FBPA, the calculation of number of disintegrations in the urinary bladder was determined considering 80 % voiding of the bladder contents at 60 and 240 min after injecting the radiotracer.

### Murine study

Animal studies were approved by the Animal Care and Use Committee of the Tokyo Metropolitan Institute of Gerontology. Male ddY mice were obtained from Tokyo Laboratory Animals (Tokyo, Japan).

Biodistribution of five radiotracers, except <sup>11</sup>C-4DST, were previously evaluated using male ddY mice [6, 8–11], and the data were used for the dosimetry calculations in the present study. A similar method was applied to the present biodistribution study of <sup>11</sup>C-4DST. In brief, <sup>11</sup>C-4DST (10 MBq/0.32 nmol) was intravenously injected into male ddY mice (8 weeks old), and the mice were euthanized by cervical dislocation at 1, 5, 15, 30, 60, and 90 min after injection (*n* = 4). Blood was collected by cardiac puncture and tissues were dissected. Leaked urine at the time of euthanasia and bladder contents were absorbed onto filter paper. The samples were measured for radioactivity with an auto-gamma counter (Wallac, Turku, Finland) and then weighed. Radioactivities and weights of urine absorbed

onto the filter papers were measured, and added to the bladder data. The radioactivity was decay corrected, and its levels in tissues were expressed as the percentage of the injected dose per g of tissue and as the percentage of the injected dose per g of organ.

For comparison with human data, the data of organs on which ROIs were placed in the human study were used; however, in the animal studies, data of the thyroid and gallbladder for all six radiotracers and data of the stomach for  $^{18}\text{F}$ -FBPA were not available. Because the weights of urine were only available for  $^{11}\text{C}$ -4DST, the mean weights for each time frame in the  $^{11}\text{C}$ -4DST experiment were used as substitutes for the urine weights of the other radiotracers. The number of disintegrations of all six radiotracers was calculated from the decay-uncorrected mean time–activity curves, as described above, and the %kg/g method [19] was used to extrapolate to a reference 70-kg adult male phantom.

#### Organ-absorbed dose and effective dose

The absorbed doses in 25 target organs of the adult male phantom were estimated from the number of disintegrations of the source organs by implementing the Medical Internal Radiation Dose (MIRD) method using OLINDA (Vanderbilt University, Nashville, TN, USA) [18]. The effective dose was also calculated by OLINDA using the methodology described in International Commission on Radiological Protection (ICRP) publications 60 [20]. For the murine study, two inputs (number of disintegrations

with and without extrapolation) were used for investigating the effect of extrapolation.

#### Results

The typical whole-body distributions of six radiotracers in human subjects are shown in Fig. 1. The typical time courses of decay-corrected radioactivity in several organs of the same subject shown in Fig. 1 are compared with those of the mice in Supplementary Fig. 1, and with the mice-derived ones extrapolated to a reference human in Fig. 2. The data for all tissues examined in the mouse study for  $^{11}\text{C}$ -4DST are summarized in Supplementary Tables 1 and 2. The data for the five other radiotracers were reported previously [6, 8–11].

In the  $^{11}\text{C}$ -SA4503 PET image, the highest peak accumulation was observed in the lungs in the first frame followed by rapid clearance. The liver showed an accumulative pattern, and uptake was highest among the organs at the latter phase. The kidneys are clearly visible at an early phase, whereas the pancreas and spleen are visible at a later phase in Fig. 1. Accumulation in the urinary bladder was much lower for  $^{11}\text{C}$ -SA4503 than for other radiotracers. Marked differences were not found in the human- and mouse-derived biodistribution data.  $^{11}\text{C}$ -MPDX and  $^{11}\text{C}$ -TMSX had similar distribution patterns with the highest uptake in the liver for the entire period; the differences between the two radiotracers were found in heart wall uptake and gallbladder uptake for  $^{11}\text{C}$ -TMSX. In the mouse-derived data, accumulations of both

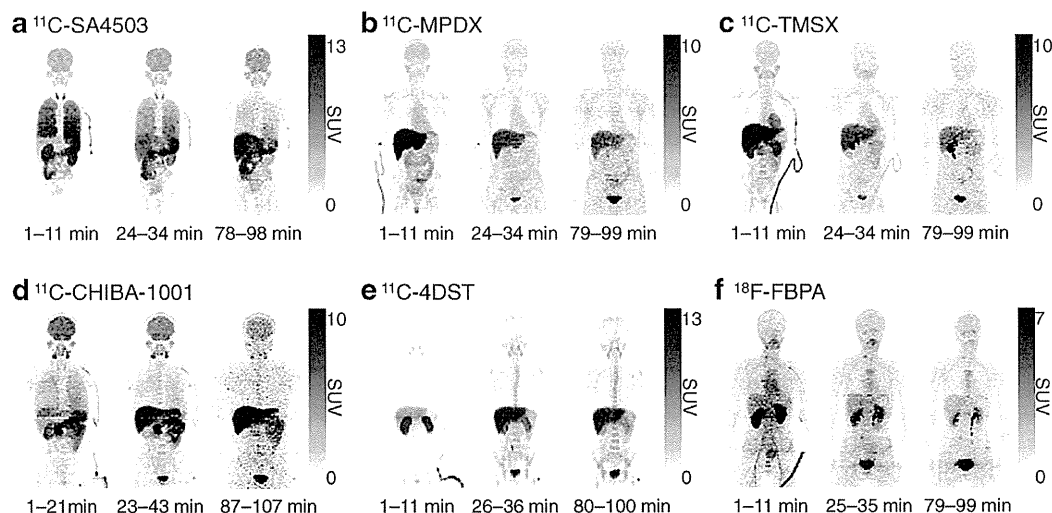


**Fig. 1** Typical whole-body distribution of radioactivity in decay-corrected maximum-intensity projection images after an intravenous radiotracer injection. The radiotracers were **a**  $^{11}\text{C}$ -SA4503, **b**  $^{11}\text{C}$ -

MPDX, **c**  $^{11}\text{C}$ -TMSX, **d**  $^{11}\text{C}$ -CHIBA-1001, **e**  $^{11}\text{C}$ -4DST, and **f**  $^{18}\text{F}$ -FBPA. **d** and **e** are images of different subjects from figures in references [7] and [6], respectively

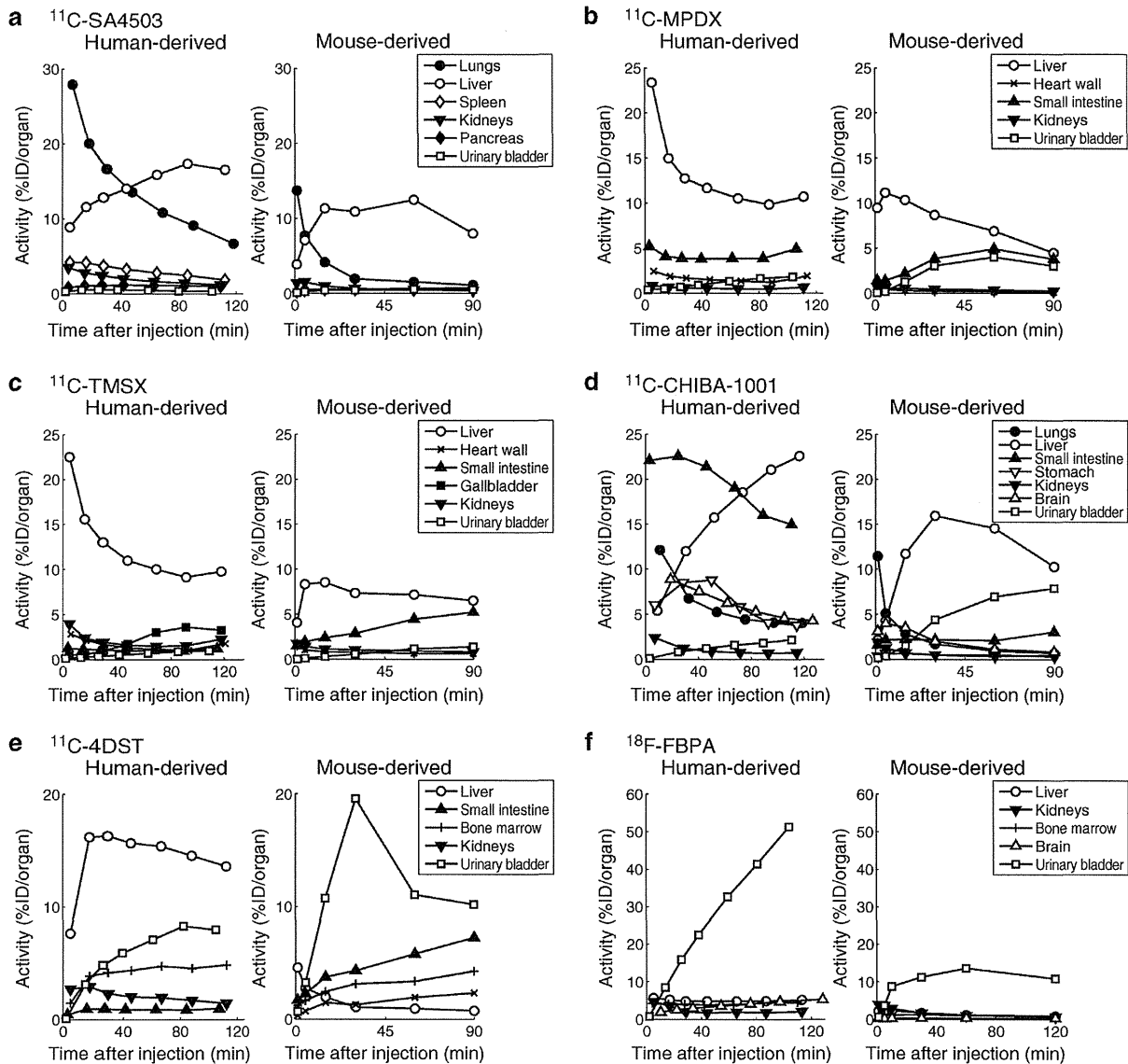


**Fig. 2** Comparison of time–activity curves of several organs in human- and mouse-derived data. Typical regional decay-corrected time–activity curves of selected organs after an intravenous injection of each radiotracer. The %kg/g method [19] was used to extrapolate the animal-derived data to a reference 70-kg adult male phantom. The

radiotracers were **a**  $^{11}\text{C}$ -SA4503, **b**  $^{11}\text{C}$ -MPDX, **c**  $^{11}\text{C}$ -TMSX, **d**  $^{11}\text{C}$ -CHIBA-1001, **e**  $^{11}\text{C}$ -4DST, and **f**  $^{18}\text{F}$ -FBPA. Data are expressed as the percentage of injected dose per organ. Selected subjects in D and E are different from the subjects in figures of references [7] and [6], respectively

$^{11}\text{C}$ -MPDX and  $^{11}\text{C}$ -TMSX in the small intestine were emphasized. For  $^{11}\text{C}$ -CHIBA-1001, marked differences were found between the human- and mouse-derived data. The measured level of uptake in the small intestine of human was much higher than that of the mouse-derived data, and excretion of the radioactive substances into the urinary bladder was much higher in mice than in human subjects. Among the six radiotracers, the most prominent difference was observed for  $^{11}\text{C}$ -4DST. The highest uptake

in human subjects was found in the liver, whereas accumulation in the small intestine was highest among mouse organs. Similar to  $^{11}\text{C}$ -CHIBA-1001, excretion of radioactive substances into the urinary bladder was much higher in mice than in human subjects. Incorporation of  $^{18}\text{F}$ -FBPA into tissues from blood was very low except in the kidneys. Of all radiotracers investigated, excretion into the urinary bladder in human subjects was fastest for  $^{18}\text{F}$ -FBPA, while it was insufficiently evaluated in the mouse-derived data.

**Table 1** Numbers of disintegrations calculated from distribution studies by dynamic whole-body PET in human and by the tissue dissection method in mice

Organs	Numbers of disintegrations (h)					
	<sup>11</sup> C-SA4503		<sup>11</sup> C-MPDX		<sup>11</sup> C-TMSX	
	Human-derived	Mouse-derived	Human-derived	Mouse-derived	Human-derived	Mouse-derived
Lungs	8.3E–02	2.1E–02	7.8E–03	5.7E–03	1.2E–02	6.2E–03
Liver	4.3E–02	4.8E–02	6.1E–02	4.5E–02	6.0E–02	3.7E–02
Brain	3.6E–02	1.1E–02	1.4E–02	4.7E–03	1.3E–02	6.1E–03
Small intestine	1.6E–02	8.7E–03	1.7E–02	1.4E–02	1.2E–02	1.4E–02
Spleen	1.5E–02	2.3E–03	*	†	*	†
Kidneys	1.4E–02	4.4E–03	2.6E–03	2.4E–03	8.6E–03	5.6E–03
Heart wall	9.9E–03	1.3E–03	9.0E–03	1.4E–03	7.7E–03	4.3E–03
Pancreas	5.5E–03	2.4E–03	*	†	*	†
Stomach	5.4E–03	1.2E–03	2.4E–03	1.3E–03	2.4E–03	9.9E–04
Thyroid	2.0E–03	‡	2.3E–04	‡	1.9E–04	‡
Urinary bladder	1.0E–03	1.9E–03	3.6E–03	9.5E–03	3.3E–03	2.5E–03
Gallbladder	*	‡	*	‡	3.1E–03	‡
Red marrow	*	†	*	†	*	†
Remainder of body	2.6E–01	3.9E–01	3.7E–01	4.1E–01	3.7E–01	4.1E–01

Organs	Numbers of disintegrations (h)					
	<sup>11</sup> C-CHIBA-1001		<sup>11</sup> C-4DST		<sup>18</sup> F-FBPA	
	Human-derived	Mouse-derived	Human-derived	Mouse-derived	Human-derived	Mouse-derived
Lungs	5.8E–02	1.5E–02	6.0E–03	4.4E–03	5.2E–02	1.4E–02
Liver	6.6E–02	5.4E–02	6.9E–02	9.0E–03	1.0E–01	3.2E–02
Brain	3.5E–02	1.3E–02	*	†	7.3E–02	8.2E–03
Small intestine	7.5E–02	1.1E–02	3.5E–03	2.0E–02	*	†
Spleen	7.3E–03	1.6E–03	3.8E–03	6.4E–03	7.5E–03	2.8E–03
Kidneys	1.2E–02	3.8E–03	1.4E–02	3.1E–03	4.2E–02	3.0E–02
Heart wall	3.1E–03	1.1E–03	2.0E–03	1.2E–03	4.2E–02	3.9E–03
Pancreas	5.2E–03	1.5E–03	*	†	*	†
Stomach	2.5E–02	2.6E–03	*	†	6.6E–03	‡
Thyroid	1.9E–04	‡	*	‡	2.1E–03	‡
Urinary bladder	3.8E–03	1.6E–02	2.3E–02	5.4E–02	4.1E–01	2.7E–01
Gallbladder	2.3E–04	‡	*	‡	*	‡
Red marrow	*	†	2.2E–02	1.3E–02	6.2E–02	2.9E–02
Remainder of body	2.0E–01	3.7E–01	3.5E–01	3.8E–01	1.8E+00	2.2E+00

Human-derived data are mean ( $n = 3$ ). Values are shown in descending order of human <sup>11</sup>C-SA4503 data

\* not identifiable, † not used in calculation, ‡ not available

The number of disintegrations in human source organs and those with and without extrapolation in the murine studies are summarized in Table 1. The number of disintegrations was much higher in many organs in human subjects than in mice with and without extrapolation in mice, with a few exceptions. The numbers of disintegrations for <sup>11</sup>C-CHIBA-1001 and <sup>11</sup>C-SA4503 in the lungs, in the small intestine for <sup>11</sup>C-CHIBA-1001, and in the liver

for <sup>11</sup>C-4DST were particularly higher in human subjects than in mice.

The organ-absorbed doses and effective doses are summarized in Tables 2 and 3, respectively. The critical organs that received the highest absorbed dose in the human- and mouse-derived studies were the same for three radiotracers: <sup>11</sup>C-TMSX, <sup>11</sup>C-4DST, and <sup>18</sup>F-FBPA. The liver and small intestine received the highest absorbed doses of <sup>11</sup>C-MPDX

**Table 2** Organ-absorbed doses and effective doses estimated from whole-body PET in human and from a tissue dissection study in mice

	Organ-absorbed dose ( $\mu\text{Gy}/\text{MBq}$ )					
	$^{11}\text{C-SA4503}$		$^{11}\text{C-MPDX}$		$^{11}\text{C-TMSX}$	
	Human-derived	Mouse-derived	Human-derived	Mouse-derived	Human-derived	Mouse-derived
Adrenals	$3.4\text{E}+00 \pm 7.9\text{E}-02$	3.3E+00	$3.3\text{E}+00 \pm 3.6\text{E}-02$	3.2E+00	$3.4\text{E}+00 \pm 1.1\text{E}-01$	3.3E+00
Brain	$8.6\text{E}+00 \pm 1.9\text{E}+00$	3.0E+00	$3.6\text{E}+00 \pm 3.6\text{E}-01$	1.5E+00	$3.3\text{E}+00 \pm 2.6\text{E}-01$	1.9E+00
Breasts	$2.1\text{E}+00 \pm 6.7\text{E}-02$	2.3E+00	$2.2\text{E}+00 \pm 5.3\text{E}-02$	2.2E+00	$2.2\text{E}+00 \pm 2.9\text{E}-02$	2.3E+00
Gallbladder wall	$3.3\text{E}+00 \pm 2.0\text{E}-01$	3.8E+00	$4.0\text{E}+00 \pm 1.8\text{E}-01$	3.8E+00	<b><math>1.1\text{E}+01 \pm 5.6\text{E}+00</math></b>	3.7E+00
LLI wall	$2.2\text{E}+00 \pm 8.5\text{E}-02$	2.9E+00	$2.9\text{E}+00 \pm 4.5\text{E}-02$	3.2E+00	$2.8\text{E}+00 \pm 2.0\text{E}-01$	3.1E+00
Small intestine	$7.0\text{E}+00 \pm 1.5\text{E}+00$	5.4E+00	<b><math>7.7\text{E}+00 \pm 9.4\text{E}-01</math></b>	<b><math>7.2\text{E}+00</math></b>	$6.4\text{E}+00 \pm 2.6\text{E}+00$	<b><math>7.1\text{E}+00</math></b>
Stomach wall	$5.6\text{E}+00 \pm 1.8\text{E}+00$	3.5E+00	$4.0\text{E}+00 \pm 5.8\text{E}-01$	3.5E+00	$4.0\text{E}+00 \pm 1.1\text{E}+00$	3.4E+00
ULI wall	$2.8\text{E}+00 \pm 1.1\text{E}-01$	3.2E+00	$3.4\text{E}+00 \pm 7.5\text{E}-02$	3.5E+00	$3.3\text{E}+00 \pm 2.6\text{E}-01$	3.5E+00
Heart wall	$1.0\text{E}+01 \pm 2.0\text{E}+00$	2.7E+00	<b><math>8.9\text{E}+00 \pm 2.6\text{E}+00</math></b>	2.7E+00	$7.9\text{E}+00 \pm 3.0\text{E}+00$	5.0E+00
Kidneys	$1.4\text{E}+01 \pm 2.4\text{E}+00$	5.5E+00	$3.9\text{E}+00 \pm 1.2\text{E}+00$	3.6E+00	<b><math>9.2\text{E}+00 \pm 2.4\text{E}+00</math></b>	<b><math>6.5\text{E}+00</math></b>
Liver	$8.4\text{E}+00 \pm 2.2\text{E}+00$	<b><math>9.0\text{E}+00</math></b>	<b><math>1.1\text{E}+01 \pm 1.9\text{E}+00</math></b>	<b><math>8.4\text{E}+00</math></b>	<b><math>1.1\text{E}+01 \pm 1.6\text{E}+00</math></b>	<b><math>7.2\text{E}+00</math></b>
Lungs	<b><math>2.2\text{E}+01 \pm 7.9\text{E}-01</math></b>	<b><math>6.6\text{E}+00</math></b>	$3.3\text{E}+00 \pm 7.7\text{E}-01$	2.7E+00	$4.4\text{E}+00 \pm 1.2\text{E}+00$	2.8E+00
Muscle	$2.1\text{E}+00 \pm 9.2\text{E}-02$	2.5E+00	$2.5\text{E}+00 \pm 5.5\text{E}-02$	2.6E+00	$2.4\text{E}+00 \pm 7.0\text{E}-02$	2.6E+00
Ovaries	$2.4\text{E}+00 \pm 6.7\text{E}-02$	3.0E+00	$3.1\text{E}+00 \pm 2.3\text{E}-02$	3.4E+00	$3.0\text{E}+00 \pm 2.4\text{E}-01$	3.3E+00
Pancreas	$1.7\text{E}+01 \pm 1.8\text{E}+00$	<b><math>8.5\text{E}+00</math></b>	$3.3\text{E}+00 \pm 3.5\text{E}-02$	3.3E+00	$3.4\text{E}+00 \pm 1.3\text{E}-01$	3.3E+00
Red marrow	$2.1\text{E}+00 \pm 5.8\text{E}-02$	2.4E+00	$2.3\text{E}+00 \pm 3.5\text{E}-02$	2.4E+00	$2.3\text{E}+00 \pm 4.6\text{E}-02$	2.5E+00
Osteogenic cells	$2.9\text{E}+00 \pm 1.4\text{E}-01$	3.6E+00	$3.5\text{E}+00 \pm 1.1\text{E}-01$	3.7E+00	$3.5\text{E}+00 \pm 1.3\text{E}-01$	3.8E+00
Skin	$1.6\text{E}+00 \pm 8.4\text{E}-02$	2.0E+00	$2.0\text{E}+00 \pm 6.0\text{E}-02$	2.1E+00	$2.0\text{E}+00 \pm 7.2\text{E}-02$	2.1E+00
Spleen	<b><math>2.4\text{E}+01 \pm 3.1\text{E}+00</math></b>	4.7E+00	$2.7\text{E}+00 \pm 4.9\text{E}-02$	2.8E+00	$2.8\text{E}+00 \pm 6.4\text{E}-02$	2.9E+00
Testes	$1.6\text{E}+00 \pm 1.3\text{E}-01$	2.4E+00	$2.3\text{E}+00 \pm 8.5\text{E}-02$	2.6E+00	$2.3\text{E}+00 \pm 1.3\text{E}-01$	2.5E+00
Thymus	$2.5\text{E}+00 \pm 8.0\text{E}-02$	2.6E+00	$2.6\text{E}+00 \pm 9.9\text{E}-02$	2.6E+00	$2.6\text{E}+00 \pm 1.7\text{E}-02$	2.7E+00
Thyroid	<b><math>2.4\text{E}+01 \pm 2.1\text{E}+01</math></b>	2.5E+00	$3.9\text{E}+00 \pm 1.6\text{E}+00$	2.6E+00	$3.4\text{E}+00 \pm 1.2\text{E}+00$	2.6E+00
Urinary bladder wall	$2.5\text{E}+00 \pm 6.8\text{E}-01$	3.9E+00	$5.0\text{E}+00 \pm 3.0\text{E}-01$	<b><math>9.2\text{E}+00</math></b>	$4.7\text{E}+00 \pm 1.1\text{E}+00$	4.5E+00
Uterus	$2.3\text{E}+00 \pm 8.4\text{E}-02$	3.1E+00	$3.2\text{E}+00 \pm 3.5\text{E}-02$	3.5E+00	$3.0\text{E}+00 \pm 2.4\text{E}-01$	3.3E+00
Total body	$2.9\text{E}+00 \pm 1.0\text{E}-02$	2.9E+00	$2.9\text{E}+00 \pm 5.3\text{E}-16$	2.9E+00	$2.9\text{E}+00 \pm 5.8\text{E}-03$	2.9E+00

Table 2 continued

	Organ-absorbed dose ( $\mu\text{Gy}/\text{MBq}$ )					
	$^{11}\text{C-CHIBA-1001}$		$^{11}\text{C-4DST}$		$^{18}\text{F-FBPA}$	
	Human-derived	Mouse-derived	Human-derived	Mouse-derived	Human-derived	Mouse-derived
Adrenals	$3.2\text{E}+00 \pm 2.3\text{E}-01$	3.2E+00	$3.5\text{E}+00 \pm 7.0\text{E}-02$	2.8E+00	$1.3\text{E}+01 \pm 1.1\text{E}+00$	1.3E+01
Brain	$8.3\text{E}+00 \pm 1.7\text{E}+00$	3.4E+00	$2.0\text{E}+00 \pm 1.2\text{E}-01$	2.2E+00	$1.4\text{E}+01 \pm 4.9\text{E}+00$	3.8E+00
Breasts	$1.7\text{E}+00 \pm 2.2\text{E}-01$	2.1E+00	$2.0\text{E}+00 \pm 8.0\text{E}-02$	2.0E+00	$8.3\text{E}+00 \pm 1.2\text{E}+00$	9.0E+00
Gallbladder wall	$4.6\text{E}+00 \pm 6.9\text{E}-01$	3.8E+00	$4.0\text{E}+00 \pm 1.7\text{E}-01$	3.0E+00	$1.3\text{E}+01 \pm 8.1\text{E}-01$	1.3E+01
LLI wall	$2.7\text{E}+00 \pm 5.2\text{E}-01$	3.0E+00	$2.9\text{E}+00 \pm 7.6\text{E}-02$	3.7E+00	$1.7\text{E}+01 \pm 1.6\text{E}+00$	1.7E+01
Small intestine	<b><math>2.4\text{E}+01 \pm 8.0\text{E}+00</math></b>	<b>6.0E+00</b>	$3.9\text{E}+00 \pm 3.2\text{E}-01$	<b>8.8E+00</b>	$1.4\text{E}+01 \pm 7.0\text{E}-01$	1.5E+01
Stomach wall	<b><math>1.6\text{E}+01 \pm 4.9\text{E}+00</math></b>	4.1E+00	$2.8\text{E}+00 \pm 7.8\text{E}-02$	2.8E+00	$1.3\text{E}+01 \pm 1.7\text{E}+00$	1.3E+01
ULI wall	$4.6\text{E}+00 \pm 1.0\text{E}+00$	3.2E+00	$3.0\text{E}+00 \pm 7.6\text{E}-02$	3.6E+00	$1.3\text{E}+01 \pm 9.0\text{E}-01$	1.4E+01
Heart wall	$4.4\text{E}+00 \pm 1.3\text{E}+00$	2.5E+00	$3.2\text{E}+00 \pm 2.3\text{E}-01$	2.2E+00	<b><math>3.0\text{E}+01 \pm 8.8\text{E}+00</math></b>	8.8E+00
Kidneys	$1.3\text{E}+01 \pm 5.1\text{E}+00$	4.9E+00	<b><math>1.4\text{E}+01 \pm 3.0\text{E}+00</math></b>	4.1E+00	<b><math>3.2\text{E}+01 \pm 1.4\text{E}+01</math></b>	<b>2.5E+01</b>
Liver	$1.2\text{E}+01 \pm 5.2\text{E}+00$	<b>1.0E+01</b>	<b><math>1.2\text{E}+01 \pm 2.3\text{E}+00</math></b>	2.4E+00	$1.7\text{E}+01 \pm 4.3\text{E}+00$	8.9E+00
Lungs	$1.6\text{E}+01 \pm 8.2\text{E}+00$	5.1E+00	$2.8\text{E}+00 \pm 5.7\text{E}-01$	2.2E+00	$1.4\text{E}+01 \pm 3.6\text{E}+00$	8.0E+00
Muscle	$1.9\text{E}+00 \pm 1.3\text{E}-01$	2.5E+00	$2.4\text{E}+00 \pm 7.9\text{E}-02$	2.6E+00	$1.1\text{E}+01 \pm 7.1\text{E}-01$	1.2E+01
Ovaries	$3.3\text{E}+00 \pm 7.0\text{E}-01$	3.2E+00	$3.0\text{E}+00 \pm 7.6\text{E}-02$	3.9E+00	$1.7\text{E}+01 \pm 1.2\text{E}+00$	1.7E+01
Pancreas	<b><math>1.7\text{E}+01 \pm 6.6\text{E}+00</math></b>	6.0E+00	$3.4\text{E}+00 \pm 3.6\text{E}-02$	3.0E+00	$1.3\text{E}+01 \pm 9.7\text{E}-01$	1.3E+01
Red marrow	$2.0\text{E}+00 \pm 1.1\text{E}-01$	2.3E+00	$4.5\text{E}+00 \pm 5.9\text{E}-01$	3.6E+00	$1.4\text{E}+01 \pm 3.6\text{E}-01$	1.3E+01
Osteogenic cells	$2.4\text{E}+00 \pm 2.0\text{E}-01$	3.5E+00	$4.6\text{E}+00 \pm 2.3\text{E}-01$	4.3E+00	$1.7\text{E}+01 \pm 1.8\text{E}+00$	1.8E+01
Skin	$1.3\text{E}+00 \pm 1.1\text{E}-01$	2.0E+00	$1.9\text{E}+00 \pm 8.9\text{E}-02$	2.0E+00	$7.9\text{E}+00 \pm 1.1\text{E}+00$	8.9E+00
Spleen	$1.3\text{E}+01 \pm 4.7\text{E}+00$	3.7E+00	$6.9\text{E}+00 \pm 1.4\text{E}+00$	<b>1.1E+01</b>	$1.4\text{E}+01 \pm 6.9\text{E}+00$	9.5E+00
Testes	$1.3\text{E}+00 \pm 1.7\text{E}-01$	2.4E+00	$2.3\text{E}+00 \pm 9.6\text{E}-02$	2.8E+00	$1.3\text{E}+01 \pm 5.7\text{E}-01$	1.4E+01
Thymus	$1.9\text{E}+00 \pm 3.0\text{E}-01$	2.5E+00	$2.4\text{E}+00 \pm 1.1\text{E}-01$	2.4E+00	$1.0\text{E}+01 \pm 1.4\text{E}+00$	1.1E+01
Thyroid	$3.1\text{E}+00 \pm 1.1\text{E}+00$	2.4E+00	$2.3\text{E}+00 \pm 1.3\text{E}-01$	2.4E+00	$2.2\text{E}+01 \pm 6.0\text{E}+00$	1.1E+01
Urinary bladder wall	$4.3\text{E}+00 \pm 2.0\text{E}+00$	<b>1.3E+01</b>	<b><math>1.8\text{E}+01 \pm 2.7\text{E}+00</math></b>	<b>3.9E+01</b>	<b><math>2.0\text{E}+02 \pm 1.3\text{E}+02</math></b>	<b>1.5E+02</b>
Uterus	$3.2\text{E}+00 \pm 6.3\text{E}-01$	3.4E+00	$3.4\text{E}+00 \pm 3.2\text{E}-02$	4.8E+00	$2.3\text{E}+01 \pm 5.9\text{E}+00$	<b>2.2E+01</b>
Total body	$2.8\text{E}+00 \pm 2.5\text{E}-02$	2.8E+00	$2.8\text{E}+00 \pm 0.0\text{E}+00$	2.7E+00	$1.2\text{E}+01 \pm 3.5\text{E}-01$	1.2E+01

Human-derived data are mean  $\pm$  S.D ( $n = 3$ ). Values of the organ receiving the first to third highest absorbed dose are in bold  
*LLI* lower large intestine, *ULI* upper large intestine

**Table 3** Effective doses estimated from whole-body PET in human and from a tissue dissection study in mice

	Effective dose ( $\mu\text{Sv}/\text{MBq}$ )		Ratio	References
	Human-derived	Mouse-derived		
$^{11}\text{C}$ -SA4503	$6.7 \pm 0.83$	3.6	1.88	This paper
$^{11}\text{C}$ -MPDX	$3.5 \pm 0.14$	3.4	1.01	This paper
$^{11}\text{C}$ -TMSX	$3.6 \pm 0.29$	3.2	1.13	This paper
$^{11}\text{C}$ -CHIBA-1001	$6.9 \pm 0.17$	4.0	1.71	[6], This paper
$^{11}\text{C}$ -4DST	$4.2 \pm 0.27$	4.8	0.86	[7], This paper
$^{11}\text{C}$ -Methoxyprogabidic acid	5.3	4.8	1.10	[3]
$^{11}\text{C}$ -Choline	4.4	2.8 (rats)	1.57	[5]
$^{18}\text{F}$ -FBPA	$23.9 \pm 7.9$	18.7	1.28	This paper
<i>O</i> -(2- $^{18}\text{F}$ -Fluoroethyl)-L-tyrosine	16.5	9.0	1.83	[22, 31]
$^{18}\text{F}$ -6-Fluoro-L-dopa	19.9	26*	0.37–0.77	[23, 25]
$^{18}\text{F}$ -FDG	19, 24*, 29			[24, 25, 32]

Human-derived data are mean  $\pm$  S.D. ( $n = 3$ )

\* Effective dose equivalents ( $\mu\text{Sv}/\text{MBq}$ ) according to ICRP publication 26

and  $^{11}\text{C}$ -CHIBA-1001, respectively, in the human studies, and received the second and third highest doses, respectively, in the murine studies; whereas the highest absorbed dose for both tracers was in the urinary bladder in the murine study. The spleen had the highest absorbed doses of  $^{11}\text{C}$ -SA4503 in the human study, while it ranked lower in the murine study; the thyroid also had the highest dose in the human study, but it could not be directly compared with that in the murine study because it was not measured in mice. When considering the ratios of human-derived data to mouse-derived data, the most underestimated organs measured in mice were the spleen for  $^{11}\text{C}$ -SA4503 (ratio = 5.0), heart wall for  $^{11}\text{C}$ -MPDX (ratio = 3.3), gallbladder wall for  $^{11}\text{C}$ -TMSX (ratio = 3.0), small intestine for  $^{11}\text{C}$ -CHIBA-1001 (ratio = 4.0), liver for  $^{11}\text{C}$ -4DST (ratio = 5.1), and brain for  $^{18}\text{F}$ -FBPA (ratio = 3.8). In contrast, the only overestimated organ in mice was the urinary bladder wall for  $^{11}\text{C}$ -CHIBA-1001 (ratio = 0.30). The standard deviations (SD) of the effective dose in the human-derived studies were small (%SD = 2.5–12.3) in the five  $^{11}\text{C}$ -labeled tracers. In contrast,  $^{18}\text{F}$ -FBPA displayed a marked variability in the effective dose among the subjects (%SD = 33.1). The effective doses of four radiotracers,  $^{11}\text{C}$ -MPDX,  $^{11}\text{C}$ -TMSX,  $^{11}\text{C}$ -4DST, and  $^{18}\text{F}$ -FBPA, in the human-derived studies were comparable to those in the mouse-derived studies, with ratios of 1.01, 1.13, 0.86, and 1.28, respectively. However, the human-derived effective doses of  $^{11}\text{C}$ -SA4503 and  $^{11}\text{C}$ -CHIBA-1001 were higher than the mouse-derived doses with ratios of 1.88 and 1.71, respectively.

## Discussion

In this study of human whole-body PET scans, the calculated effective doses of the five  $^{11}\text{C}$ -labeled radiotracers

investigated were within the range of 28 other  $^{11}\text{C}$ -labeled PET radiotracers (3.2–14.1  $\mu\text{Sv}/\text{MBq}$ ) [2, 5, 21], and the effective dose of  $^{18}\text{F}$ -FBPA was similar to that of *O*-(2- $^{18}\text{F}$ -fluoroethyl)-L-tyrosine [22],  $^{18}\text{F}$ -6-fluoro-L-dopa [23], and  $^{18}\text{F}$ -FDG [24, 25]. When mouse-derived (with extrapolation) and human-derived effective doses were compared, the results for  $^{11}\text{C}$ -MPDX,  $^{11}\text{C}$ -TMSX, and  $^{18}\text{F}$ -FBPA were comparable, but the mouse-derived values from  $^{11}\text{C}$ -CHIBA-1001 and  $^{11}\text{C}$ -SA4503 were >40 %, but less than the human-derived values. Despite the prominent differences in the whole-body distributions of  $^{11}\text{C}$ -4DST in human subjects and mice, a marked difference was not found in the human- and mouse-derived effective doses (4.2 vs. 4.8  $\mu\text{Sv}/\text{MBq}$ ). A noteworthy finding is that the critical organs with the highest absorbed doses are not always the same as those observed for  $^{11}\text{C}$ -SA4503, for which the highest absorbed doses are estimated in the spleen in the human study and in the liver in the murine study.

Several reasons have been proposed for the discrepancies between mouse- and human-derived organ-absorbed doses. Differences in anatomy and size are probably the most obvious. In general, relative organ size decreases as animal size increases. This may affect the rate of tracer elimination, because the levels of hepatic enzymes and the number of nephrons as a fraction of kidney weight are thought to be higher in mice than in human subjects [26]. In addition, biliary excretion and bladder exposure vary substantially between species, and blood circulation time is shorter in mice than in human subjects. This high systemic circulation rate and elimination rate in small animals may be responsible for the smaller mouse-derived effective doses of  $^{11}\text{C}$ -SA4503 and  $^{11}\text{C}$ -CHIBA-1001 than those observed in human subjects. Theoretically, the glomerular

filtration rate ratio between human and animals can be used to predict renal excretion of drugs in human subjects. Similarly, when the elimination of a drug mainly occurs in the liver and the rate of elimination is limited by hepatic blood flow, the clearance of the tracer in human subjects can be predicted by the hepatic blood flow. However, biochemical parameters, such as protein binding, characteristics of the blood–brain barrier, and drug metabolism, are less predictable. These parameters vary considerably among species. Therefore, in the mouse- and human-derived estimations only half of the tracers were matched in their most critical organs. The urinary bladder wall was the most critical organ for the tracers in the mouse-derived studies, with the exception of  $^{11}\text{C}$ -SA4503 and  $^{11}\text{C}$ -TMSX. For example, metabolite analysis of  $^{11}\text{C}$ -4DST indicated that  $^{11}\text{C}$ -4DST was stable in mice [27], but some amount of  $^{11}\text{C}$ -4DST was glucuronidated in the human body [7]. The presence of a radioactive glucuronidated metabolite was consistent with the high uptake of radioactive substances in the human liver, which is inconsistent with the low uptake in the mouse liver. Similarly,  $^{11}\text{C}$ -CHIBA-1001 has a tertiary amine which is *N*-glucuronidated in non-human primates and human subjects. Bile excretion of *N*-glucuronidated metabolite(s) of  $^{11}\text{C}$ -CHIBA-1001 may occur in human subjects [28], and may be supported by hepatobiliary excretion. In mice, enzymatic oxidation of  $^{11}\text{C}$ -CHIBA-1001 may occur which would be supported by the relatively higher uptake of  $^{11}\text{C}$ -CHIBA-1001 in the kidneys and urinary bladder. Regarding metabolism of  $^{11}\text{C}$ -labeled radiotracers, it is possible that rates of expiration of  $^{11}\text{C}$ -CO<sub>2</sub>, which were not evaluated in either the human or animal studies, may produce discrepancies between the human- and animal-derived radiation dosimetry estimates.

The methodology for the measurements of the organ radioactivities was also a factor that caused differences in the estimated radiation doses between species. Inevitable blood loss from dissected organs leads to underestimation of organ radioactivity levels, particularly in cases in which the blood levels are higher than that in organs. In the current study, the first-pass uptake of  $^{11}\text{C}$ -SA4503 and  $^{11}\text{C}$ -CHIBA-1001 was higher in the lungs among the human organs, but could not be measured in mice. This difference made the absorbed doses in the lungs much lower in the mouse-derived results. Although urine was recovered by absorbing onto filter paper in the murine studies, the dissection may have produced extensive errors in some cases; for example, in case of  $^{11}\text{C}$ -4DST and  $^{18}\text{F}$ -FBPA. Animal PET studies using a high-resolution scanner might diminish the differences due to the methodology used for measurements. For example, dynamic whole-body scans of Sprague–Dawley rats successfully measured a peak of the first-pass uptake of  $^{11}\text{C}$ -PK11195 in the lungs [29]. However, identification of small organs and/or their separation

from surrounding organs was difficult because of the limited resolution. Furthermore, the combinations of organs used as source organs for calculating the dosimetry required careful consideration. In this study, we intended to use the same combinations whenever possible, but absence of gallbladder and thyroid data in the murine studies affected the absorbed doses; for example, the mouse-derived absorbed doses of  $^{11}\text{C}$ -TMSX in the gallbladder and of  $^{11}\text{C}$ -SA4503 in the thyroid were much lower than the human-derived absorbed doses.

Pharmacokinetically,  $^{18}\text{F}$ -FBPA is not incorporated in to proteins as *O*-(2- $^{18}\text{F}$ -fluoroethyl)-L-tyrosine [23] and  $^{18}\text{F}$ -6-fluoro-L-dopa [25]. It is noted that these three artificial amino acids and  $^{18}\text{F}$ -FDG were rapidly cleared into the urinary bladder via the kidneys, with some retention in tumors or in the brain. Therefore, the absorbed dose at the urinary bladder wall was much higher than in other organs. The unnecessary bladder dose of these  $^{18}\text{F}$ -labeled tracers can be reduced by certain strategies, such as hydration and frequent voiding. These  $^{18}\text{F}$ -fluorinated analogs of natural substrates showed similar pharmacokinetics in human and rodents, and the effective doses were similarly estimated from both human- and rodent-derived studies [25]. An effective dose approximately two times higher (53.9  $\mu\text{Sv}/\text{MBq}$ ) was reported for  $^{18}\text{F}$ -6-fluoro-L-dopa in a dog-derived study [30]. The L-form of  $^{18}\text{F}$ -FBPA was used in the present clinical study, while the D- and L-form was used in the previous distribution study in mice [15]. However, these differences might not have significantly affected the results, because both the L- and D-forms of  $^{18}\text{F}$ -FBPA are metabolically stable and are rapidly cleared from the body to the urinary bladder.

Unlike the other five tracers,  $^{18}\text{F}$ -FBPA displayed marked variability in the effective dose among the subjects.  $^{18}\text{F}$ -FBPA was excreted rapidly in urine, which in turn considerably affected the estimated effective dose. Generally, dose estimations for organs involved in excretory pathways displayed a marked variability among the subjects. In addition, although renal functions of two patients with brain tumors were normal in the  $^{18}\text{F}$ -FBPA PET study, one patient was given several therapeutic drugs including prednisolone, which could enhance urination. These factors could be responsible for a marked difference in the effective dose estimations of individual subjects.

Accordingly, the results indicated that extrapolation experiments using mice with accommodation for differences in organ to total body mass proportions were often not beneficial in predicting dosimetry in human subjects. These findings emphasized that human dosimetry studies for radiation risk assessment are necessary for the initial clinical evaluation of new PET radiotracers. However, preclinical animal studies are required to determine whether the radiotracers focally accumulate in particular organs



such as  $^{18}\text{F}$ -FBPA in the urinary bladder, particularly for tracers with longer half-lives.

## Conclusion

In this study, we investigated the biodistribution, pharmacokinetics, and radiation dosimetry of six radiotracers for PET in human subjects, and compared the results with those from murine studies. The estimated effective doses of four radiotracers in the human studies were roughly comparable to those estimated in the mouse-derived studies with ratios of human to mouse data ranging from 0.86 to 1.28; whereas the ratios of  $^{11}\text{C}$ -CHIBA-1001 and  $^{11}\text{C}$ -SA4503 were 1.71 and 1.88, respectively. Regardless of the similar effective doses, the pharmacokinetics of  $^{11}\text{C}$ -4DST proved to be considerably different between human subjects and mice, and in the case of  $^{11}\text{C}$ -SA4503, the critical organ with the maximum absorbed dose was different between the human- and mouse-derived studies. Interspecies differences in pharmacokinetics between human subjects and mice and differences in the methodology of biodistribution measurements were considered to be the main factors responsible for inconsistencies between the human- and mouse-derived estimates. Thus, whole-body imaging for the investigation of radiation dosimetry is recommended as an initial clinical trial when evaluating new PET probes prior to their application in subsequent clinical investigations.

**Acknowledgments** This work was supported by Grants-in-Aid for Scientific Research (C) No. 19591665 (Tadashi Nariai), (B) No. 22390241 (Jun Toyohara), and (B) No. 20390334 (Kiichi Ishiwata) from the Japan Society for the Promotion of Science, and a Grant from the National Center for Global Health and Medicine (Jun Toyohara, Tadashi Nariai, and Kiichi Ishiwata).

## References

- Zanotti-Fregonara P, Innis RB. Suggested pathway to assess radiation safety of  $^{11}\text{C}$ -labeled PET tracers for first-in-human studies. *Eur J Nucl Med Mol Imaging*. 2012;39:544–7.
- van der Aart J, Hallett WA, Rabiner EA, Passchier J, Comley RA. Radiation dose estimates for carbon-11-labelled PET tracers. *Nucl Med Biol*. 2012;39:305–14.
- Santens P, De Vos F, Thierens H, et al. Biodistribution and dosimetry of carbon-11-methoxyprogabidic acid, a possible ligand for GABA-receptors in the brain. *J Nucl Med*. 1998;39:307–10.
- Bencherif B, Endres CJ, Musachio JL, et al. PET imaging of brain acetylcholinesterase using  $^{11}\text{C}$ CP-126,998, a brain selective enzyme inhibitor. *Synapse*. 2002;45:1–9.
- Tolvanen T, Yli-Kerttula T, Ujula T, et al. Biodistribution and radiation dosimetry of  $^{11}\text{C}$ choline: a comparison between rat and human data. *Eur J Nucl Med Mol Imaging*. 2010;37:874–83.
- Sakata M, Wu J, Toyohara J, et al. Biodistribution and radiation dosimetry of the  $\alpha_7$  nicotinic acetylcholine receptor ligand  $^{11}\text{C}$ CHIBA-1001 in humans. *Nucl Med Biol*. 2011;38:443–8.
- Toyohara J, Nariai T, Sakata M, et al. Whole-body distribution and brain tumor imaging with  $^{11}\text{C}$ -4DST: a pilot study. *J Nucl Med*. 2011;52:1322–8.
- Kawamura K, Ishiwata K, Shimada Y, et al. Preclinical evaluation of  $^{11}\text{C}$ SA4503: radiation dosimetry, in vivo selectivity and PET imaging of  $\sigma_1$  receptors in the cat brain. *Ann Nucl Med*. 2000;14:285–92.
- Ishiwata K, Nariai T, Kimura Y, et al. Preclinical studies on  $^{11}\text{C}$ MPDX for mapping adenosine  $A_1$  receptors by positron emission tomography. *Ann Nucl Med*. 2002;16:377–82.
- Ishiwata K, Wang WF, Kimura Y, Kawamura K, Ishii K. Preclinical studies on  $^{11}\text{C}$ JTMSX for mapping adenosine  $A_2A$  receptors by positron emission tomography. *Ann Nucl Med*. 2003;17:205–11.
- Ishiwata K, Ido T, Mejia AA, Ichihashi M, Mishima Y. Synthesis and radiation dosimetry of 4-borono-2- $^{18}\text{F}$ fluoro-D, L-phenylalanine: a target compound for PET and boron neutron capture therapy. *Appl Radiat Isot*. 1991;42:325–8.
- Kawamura K, Ishiwata K, Tajima H, et al. In vivo evaluation of  $^{11}\text{C}$ SA4503 as a PET ligand for mapping CNS  $\sigma_1$  receptors. *Nucl Med Biol*. 2000;27:255–61.
- Ishiwata K, Noguchi J, Wakabayashi S, et al.  $^{11}\text{C}$ -labeled KF18446: a potential central nervous system adenosine  $A_{2a}$  receptor ligand. *J Nucl Med*. 2000;41:345–54.
- Toyohara J, Sakata M, Wu J, et al. Preclinical and the first clinical studies on  $^{11}\text{C}$ CHIBA-1001 for mapping  $\alpha_7$  nicotinic receptors by positron emission tomography. *Ann Nucl Med*. 2009;23:301–9.
- Ishiwata K, Ishii S, Senda M, Tsuchiya Y, Tomimoto K. Electrophilic synthesis of 6- $^{18}\text{F}$ fluoro-L-DOPA: use of 4-O-pivaloyl-L-DOPA as a suitable precursor for routine production. *Appl Radiat Isot*. 1993;44:755–9.
- Fujiwara T, Watanuki S, Yamamoto S, et al. Performance evaluation of a large axial field-of-view PET scanner: SET-2400 W. *Ann Nucl Med*. 1997;11:307–13.
- Meikle SR, Bailey DL, Hooper PK, et al. Simultaneous emission and transmission measurements for attenuation correction in whole-body PET. *J Nucl Med*. 1995;36:1680–8.
- Stabin MG, Sparks RB, Crowe E. OLINDA/EXM: the second generation personal computer software for internal dose assessment in nuclear medicine. *J Nucl Med*. 2005;46:1023–7.
- Kirschner AS, Ice RD, Beierwaltes WH. Radiation dosimetry of  $^{131}\text{I}$ -19-iodocholesterol: the pitfalls of using tissue concentration data—reply. *J Nucl Med*. 1975;16:248–9.
- International Commission on Radiological Protection. ICRP Publication 60: 1990 recommendations of the International Commission on Radiological Protection. *Ann ICRP*. 1991;21:493–502.
- Hirvonen J, Roivainen A, Virta J, Helin S, Nagren K, Rinne JO. Human biodistribution and radiation dosimetry of  $^{11}\text{C}$ -(R)-PK11195, the prototypic PET ligand to image inflammation. *Eur J Nucl Med Mol Imaging*. 2010;37:606–12.
- Pauleit D, Floeth F, Herzog H, et al. Whole-body distribution and dosimetry of O-(2- $^{18}\text{F}$ fluoroethyl)-L-tyrosine. *Eur J Nucl Med Mol Imaging*. 2003;30:519–24.
- Brown WD, Oakes TR, DeJesus OT, et al. Fluorine-18-fluoro-L-DOPA dosimetry with carbidopa pretreatment. *J Nucl Med*. 1998;39:1884–91.
- Deloar HM, Fujiwara T, Shidahara M, et al. Estimation of absorbed dose for 2- $^{18}\text{F}$ fluoro-2-deoxy-D-glucose using whole-body positron emission tomography and magnetic resonance imaging. *Eur J Nucl Med*. 1998;25:565–74.

25. Mejia AA, Nakamura T, Itoh M, et al. Absorbed dose estimates in positron emission tomography studies based on the administration of  $^{18}\text{F}$ -labeled radiopharmaceuticals. *J Radiat Res.* 1991;32: 243–61.
26. Lin JH. Species similarities and differences in pharmacokinetics. *Drug Metab Dispos.* 1995;23:1008–21.
27. Toyohara J, Okada M, Toramatsu C, Suzuki K, Irie T. Feasibility studies of  $4'$ -[methyl- $^{11}\text{C}$ ]thiothymidine as a tumor proliferation imaging agent in mice. *Nucl Med Biol.* 2008;35:67–74.
28. Chiu SH, Huskey SW. Species differences in *N*-glucuronidation. *Drug Metab Dispos.* 1998;26:838–47.
29. Luoto P, Laitinen I, Suilamo S, Nāgren K, Roivainen A. Human dosimetry of carbon-11 labeled *N*-butan-2-yl-1-(2-chlorophenyl)-*N*-methylisoquinoline-3-carboxamide extrapolated from whole-body distribution kinetics and radiometabolism in rats. *Mol Imaging Biol.* 2010;12:435–42.
30. Harvey J, Firna G, Garnett ES. Estimation of the radiation dose in man due to 6-[ $^{18}\text{F}$ ]fluoro-L-dopa. *J Nucl Med.* 1985;26:931–5.
31. Tang G, Wang M, Tang X, Luo L, Gan M. Pharmacokinetics and radiation dosimetry estimation of *O*-(2-[ $^{18}\text{F}$ ]fluoroethyl)-L-tyrosine as oncologic PET tracer. *Appl Radiat Isot.* 2003;58:219–25.
32. International Commission on Radiological Protection. ICRP Publication 80. Recalculated dose data for 19 frequently used radiopharmaceuticals from ICRP Publication 53. *Ann ICRP.* 1998;28:47–83.

Clinical Investigation: Central Nervous System Tumor

## Delayed Complications in Patients Surviving at Least 3 Years After Stereotactic Radiosurgery for Brain Metastases

Masaaki Yamamoto, MD,<sup>\*,†</sup> Takuya Kawabe, MD,<sup>\*,‡</sup> Yoshinori Higuchi, MD,<sup>§</sup>  
Yasunori Sato, PhD,<sup>||</sup> Tadashi Nariai, MD,<sup>¶</sup> Bierta E. Barfod, MD,<sup>\*</sup>  
Hidetoshi Kasuya, MD,<sup>†</sup> and Yoichi Urakawa, MD<sup>\*</sup>

*\*Katsuta Hospital Mito GammaHouse, Hitachi-naka; †Department of Neurosurgery, Tokyo Women's Medical University Medical Center East, Tokyo; ‡Department of Neurosurgery, Kyoto Prefectural University of Medicine Graduate School of Medical Sciences, Kyoto; §Department of Neurosurgery and ||Clinical Research Center, Chiba University Graduate School of Medicine, Chiba; and ¶Department of Neurosurgery, Graduate School, Tokyo Medical and Dental University School of Medicine, Tokyo, Japan*

Received Mar 16, 2012, and in revised form Apr 5, 2012. Accepted for publication Apr 6, 2012

### Summary

This retrospective investigation analyzed delayed complications in patients with brain metastases treated with stereotactic radiosurgery (SRS). Among 167 brain metastasis patients surviving more than 3 years after SRS, 17 (10.2%) experienced delayed complications occurring 24.0-121.0 months (median, 57.5 months) after SRS. The actuarial incidences of delayed complications estimated by competing risk analysis were 4.2% at the 60th month and 21.2% at the 120th month after SRS. Among various clinical

**Purpose:** Little is known about delayed complications after stereotactic radiosurgery in long-surviving patients with brain metastases. We studied the actual incidence and predictors of delayed complications.

**Patients and Methods:** This was an institutional review board-approved, retrospective cohort study that used our database. Among our consecutive series of 2000 patients with brain metastases who underwent Gamma Knife radiosurgery (GKRS) from 1991-2008, 167 patients (8.4%, 89 women, 78 men, mean age 62 years [range, 19-88 years]) who survived at least 3 years after GKRS were studied.

**Results:** Among the 167 patients, 17 (10.2%, 18 lesions) experienced delayed complications (mass lesions with or without cyst in 8, cyst alone in 8, edema in 2) occurring 24.0-121.0 months (median, 57.5 months) after GKRS. The actuarial incidences of delayed complications estimated by competing risk analysis were 4.2% and 21.2% at the 60th month and 120th month, respectively, after GKRS. Among various pre-GKRS clinical factors, univariate analysis demonstrated tumor volume-related factors: largest tumor volume (hazard ratio [HR], 1.091; 95% confidence interval [CI], 1.018-1.154;  $P = .0174$ ) and tumor volume  $\leq 10$  cc vs  $> 10$  cc (HR, 4.343; 95% CI, 1.444-12.14;  $P = .0108$ ) to be the only significant predictors of delayed complications. Univariate analysis revealed no correlations between delayed complications and radiosurgical parameters (ie, radiosurgical doses, conformity and gradient indexes, and brain volumes receiving  $> 5$  Gy and  $> 12$  Gy). After GKRS, an area of prolonged enhancement at the irradiated lesion was shown to be a possible risk factor for the development of delayed complications (HR, 8.751; 95% CI, 1.785-157.9;  $P = .0037$ ). Neurosurgical interventions were performed in 13 patients (14 lesions) and mass removal for 6 lesions and Ommaya reservoir placement for the other 8. The results were favorable.

Reprint requests to: Masaaki Yamamoto, MD, Katsuta Hospital Mito GammaHouse, 5125-2 Nakane, Hitachi-naka, Ibaraki 312-0011 Japan. Tel:

(+81) 29-271-0011; Fax: (+81) 29-274-1475; E-mail: BCD06275@nifty.com

Conflict of interest: none.

Int J Radiation Oncol Biol Phys, Vol. 85, No. 1, pp. 53-60, 2013  
0360-3016/\$ - see front matter © 2013 Elsevier Inc. All rights reserved.  
doi:10.1016/j.ijrobp.2012.04.018

factors before SRS, the only significant predictors of delayed complications were volume-related factors.

**Conclusions:** Long-term follow-up is crucial for patients with brain metastases treated with GKRS because the risk of complications long after treatment is not insignificant. However, even when delayed complications occur, favorable outcomes can be expected with timely neurosurgical intervention. © 2013 Elsevier Inc.

## Introduction

Brain metastases, a common neurologic problem, are life-threatening for cancer patients in the absence of effective treatment. Recently, stereotactic radiosurgery (SRS) has become an established treatment option for brain metastases (1). SRS is more advantageous than other treatment options (ie, whole brain radiation therapy [WBRT], surgery, systemic anticancer agents, and combinations of these modalities) in terms of costs, hospitalization, morbidity, mortality, and wider applicability and repeatability (2). Although numerous prospective or retrospective series, as extensively reviewed by McDermott and Sneed (2), have reported the results of local control, survival, and/or complications in patients with brain metastases treated by SRS, little is known about delayed complications in long-surviving patients with brain metastases after SRS. We previously reported 8 patients with brain metastases and delayed cyst formation detected by magnetic resonance imaging (MRI) more than 3 years after Gamma Knife radiosurgery (GKRS) (3). Herein, we present post-GKRS delayed complications, including those of the cases described in our prior publication, and we clarify the actual incidence, clinical factors, and radiosurgical parameters predicting delayed complications. In this study, delayed complications were defined as Radiation Therapy Oncology Group (RTOG) neurotoxicity grade 2 or worse occurring more than 2 years after GKRS (4). Also, even patients with grade 0 delayed complications were included if neurosurgical intervention was required. Furthermore, we discuss the treatment and pathogenesis of these complications based on histopathologic studies.

## Methods and Materials

### Patient population

This was an institutional review board (IRB)-approved, retrospective cohort study using our database (IRB #1981). Among our consecutive series of 2000 patients with brain metastases who underwent GKRS between July 1991 and June 2008, 167 (8.4%) who survived for at least 3 years after GKRS were studied. Table 1 summarizes their clinical characteristics. The patients in our series underwent GKRS alone, without WBRT, for newly diagnosed or recurrent brain metastases after WBRT or surgery. In our facility, all patients had been referred to us for GKRS by their primary physicians. Therefore, patient selection had mostly been made outside of our facilities. The patient selection criteria may well have differed somewhat among the referring physicians. Therefore, the first author (M.Y.) ultimately decided whether or not a patient would be accepted for GKRS in all cases. Therefore, as shown in Table 1, only 1 patient was categorized into recursive partitioning analysis class 3 (5).

The treatment strategy was explained in detail to each patient and at least 1 of their adult relatives by the first author (M.Y.), and written informed consent was obtained from all patients before GKRS. Standard, single-session GKRS was performed. The

selected tumor periphery doses ranged from 10.0 Gy-25.0 Gy (median, 24.0 Gy). Excluding 1 deceased patient (patient 8), the remaining 5 agreed to the use of their histopathologic photographs for this publication.

### Discriminating local recurrence from delayed complications

The criteria for local recurrence (recurrence of the GKRS-irradiated lesion) were usually an increase in the size of the enhanced area on postgadolinium T1-weighted MRI, an enlarged tumor core on T2-weighted MR images, and the detection of a high choline peak on proton MR spectrograms. However, in some cases in which MRI raised a suspicion of recurrence, methionine positron emission tomography (PET) was used for determining whether or not the tumor had recurred. These PET examinations were performed and the results were evaluated by 1 of the authors (TN) who was not involved in either GKRS treatment or patient follow-up.

### Statistical analysis

All data were analyzed according to the intention-to-treat principle. For baseline variables, summary statistics were constructed that used frequencies and proportions for categorical data, means, and standard deviations for continuous variables. We compared patient characteristics using Fisher's exact test for categorical outcomes and *t* tests for continuous variables, as appropriate.

For time-to-event outcomes, the cumulative incidence of delayed complications was estimated by a competing risk analysis, because death is a competing risk for loss to follow-up (ie, patients who die can no longer become lost to follow-up) (6). Also, to identify the baseline and clinical variables associated with delayed complications, univariate competing risk analysis was performed with the Fine-Gray generalization of the proportional hazards model, which accounts for death as a competing risk (7).

All comparisons were planned, and the tests were 2-sided. A *P* value less than .05 was considered to indicate a statistically significant difference. One of the authors (Y.H.) initially cleaned and finalized the database using JMP, Japanese version 9.0 for the Windows system (SAS Institute, Inc., Cary, NC). Thereafter, the other author (Y.S.) independently performed statistical analyses using the SAS software program, version 9.2 (SAS Institute, Inc.) and the R statistical program, version 2.13. These 2 authors were not involved in either GKRS treatment or patient follow-up.

## Results

### Overall survival and salvage treatment

The overall median survival time after GKRS was 7.3 months (95% confidence interval [CI], 6.9-7.8 months) in our cohort of

**Table 1** Clinical characteristics of brain metastasis patients

Categories	Overall	Complication(s)		P values*
		(+)	(-)	
No. of patients	167	17	150	
Mean age (y)	62	60	62	.3855
Range	19-88	35-71	19-88	
Sex				
Female	89	9 (53%)	80 (53%)	1.000
Male	78	8	70	
Primary cancer				
Lung	101	12 (71%)	89 (59%)	.4405
Nonlung	66	5	61	
Primary cancer, Controlled	124	15 (88%)	109 (73%)	.2432
Extracranial METs, No	118	13 (76%)	105 (70%)	.7801
KPS				
≥80%	160	16 (94%)	144 (96%)	.5352
≤70%	7	1	6	
RPA class				
I	49	8	41	
II	117	9 (53%)	108 (72%)	.1593 <sup>†</sup>
III	1	0	1	
Neurologic symptoms	97	11 (65%)	86 (57%)	.6439
Prior surgery	45	3 (18%)	42 (28%)	.5645
Prior WBRT	4	1 (6%)	3 (2%)	.3342
Tumor numbers				
Mean	3	4	3	.4599
Range	1-36	1-29	1-36	
Solitary	91	9 (53%)	82 (55%)	1.000
Tumor volume (cc) <sup>‡</sup>				
Mean	4.13	7.03	3.80	.0152
Range	0.02-30.30	0.35-20.60	0.02-30.30	
≤10 cc	145	11	134	
>10 cc	22	6 (35%)	16 (11%)	.0124
Peripheral dose (Gy)				
Mean	22.0	21.4	22.1	.3209
Range	10.0-25.0	15.0-25.0	10.0-25.0	
Tumor nature				
Solid	125	14	112	
Cystic	42	3 (18%)	39 (25%)	.7663
Peritumoral edema	58	7 (42%)	51 (34%)	.5960
Accompanying hemorrhage	12	0	12 (8%)	.6139
Prolonged enhanced area <sup>§</sup>	93	16 (94%)	77 (57%)	.0028

Abbreviations: KPS = Karnofsky performance status; RPA = recursive partitioning analysis; WBRT = whole brain radiation therapy.

\* Student's *t* test was used for continuous variables and Fisher's exact test for pairs of categorical variables.

<sup>†</sup> RPA class II vs classes I and III.

<sup>‡</sup> Tumors causing delayed complications in the complication (+) group and the largest tumors in the complication (-) group.

<sup>§</sup> Demonstrated on magnetic resonance imaging (MRI) performed at the 12th post-treatment month or later (16 patients were excluded because MRI results were not available).

2000 patients. In the subset reported herein, the median post-GKRS follow-up time among censored observations was 49.9 months (range, 36.0-142.0 months), and 92 patients (55.1%) had died as of the end of July 2011. The median survival time after GKRS was 61.8 months (95% CI, 56.3-68.4 months). The actuarial post-GKRS survival rates were 52.7% at 60 months and 28.0% at 120 months after GKRS. The causes of death could not be determined in 4 patients but were confirmed in the remaining 88 to be nonbrain diseases in 72 (81.8%) and brain diseases in 16 (18.2%). Although no further salvage GKRS was required in 68 patients (40.7%), 99 (59.3%) underwent salvage GKRS mostly for newly developed

lesions and/or, rarely, recurrence of the treated lesions: twice in 47 patients, 3 times in 24, 4 times in 13, and 5 times or more in 15 (maximum, 8 times). Four patients also underwent surgical removal because of recurrence of the irradiated lesion, and 5 received WBRT for meningeal dissemination.

### Incidence and treatment of delayed complications

Among these 167 patients, 17 (10.2%) experienced delayed complications occurring 24-121 months (median, 53 months) after

**Table 2** Patients with delayed complications

Patient	Age/sex	Origin	Tumor, no/vol (cc)	Dose (Gy), min/max	RTOG grade	MRI findings	Onset (mo after GKRS)	Treatment	Post-GKRS salvage
1*	63/F	Lung (ad)	1/9.2	15.0/30.0	4	Edema	40	Medical treatment	None
2	66/F	Lung (ad)	1/2.3	25.0/29.4	3	Mass with cyst	121	Op recommended, but refused	None
3	70/F	Breast	1/6.2	20.0/40.0	0	Mass with cyst (left) cyst (right)	48	Removal ORP	GKRS
4	58/M	Lung (ad)	2/1.6	25.0/50.0	2	Cyst	48	ORP	GKRS
5	70/F	Lung (ad)	2/19.6	20.0/40.0	4	Mass with cyst	60	Op recommended, but refused	GKRS
6	66/M	Lung (scc)	1/0.6	22.0/44.0	2	Mass with cyst	105	Removal	GKRS
7	63/F	Ovary	4/11.3	20.0/33.3	0	Cyst	58	ORP	GKRS
8	71/M	Lung (ad)	1/0.4	25.0/27.8	3	Mass	44	Removal	None
9	42/M	Kidney	1/2.0	24.0/40.0	3	Cyst	71	ORP	GKRS
10	69/F	Lung (ad)	10/3.2	20.0/33.3	4	Edema	52	Medical treatment	GKRS
11	63/F	Lung (ad)	4/1.2	25.0/50.0	0	Mass with cyst	112	Removal	None
12	55/M	Lung (sq)	2/5.0	20.0/40.0	0	Cyst	105	ORP	None
13	59/F	Lung (ad)	2/10.9	21.0/35.0	0	Mass with cyst	102	Removal	None
14	35/M	Lung (ad)	1/11.1	21.0/35.0	2	Mass	27	Removal	None
15	54/M	Lung (ad)	4/3.2	24.0/40.0	0	Cyst	53	ORP	GKRS
16	46/F	Breast	29/20.6	15.0/30.0	3	Cyst	24	ORP	GKRS
17	62/M	Pharynx	1/13.1	21.0/35.0	0	Cyst	50	ORP	None

Abbreviations: ad = adenocarcinoma; GKRS = Gamma Knife radiosurgery; max = maximum; min = minimum; mo = months; MRI = magnetic resonance imaging; Op = operation; ORP = Ommaya reservoir placement; scc = small cell carcinoma; sq = squamous cell carcinoma; vol = volume.

\* This patient had undergone whole brain radiation therapy before GKRS.

GKRS, as shown in Table 2. In the 17 patients, although no further salvage GKRS was required in 8 patients, 9 underwent salvage GKRS. In 1 patient (patient 3), cyst formation occurred in the areas of 2 lesions, 1 with a mass on the left side and the other with no masses. Among a total of 18 lesions, mass lesions occurred in

6, 6 with and 2 without associated cyst, a simple cyst in 8, and extensive edema in the other 2. As shown in Fig. 1, the actuarial incidences of delayed complications estimated with competing risk analysis were 4.2% and 21.2% at the 60th month and 120th month, respectively, after GKRS. Although, as described below,

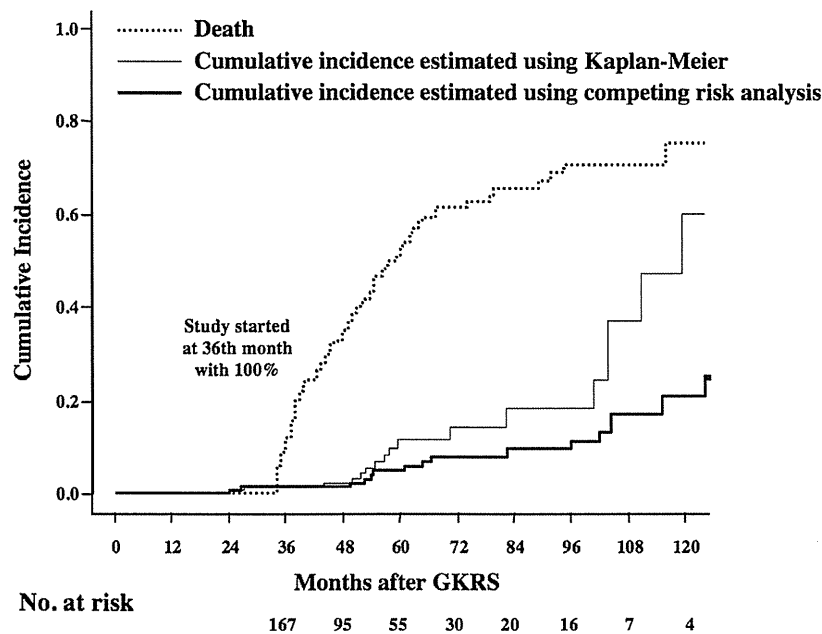


**Fig. 1.** Cumulative incidence of delayed complications after Gamma Knife radiosurgery (GKRS) estimated by the Kaplan-Meier method vs competing risk analysis.



7 patients were asymptomatic, the other 10 experienced various neurologic symptoms; 3 with RTOG neurotoxicity grade 2, 4 with grade 3, and 3 with grade 4 (4).

One patient (patient 1) who had undergone WBRT with a total dose of 50 Gy before GKRS experienced a progressive decrease in neurocognitive function (NCF). Although this patient was treated medically, NCF progressively deteriorated, and she ultimately died because of malnutrition-induced emaciation, as previously reported in detail including autopsy findings (8). Another patient (patient 10) experienced severe steroid-refractory edema. Expanding mass lesions with cyst formation were demonstrated by sequential MRI studies in 2 patients (patients 2 and 5). Although we strongly recommended surgical intervention for these patients, both refused and received only medical treatment. Their symptoms showed no amelioration. In the 12 remaining patients (13 lesions), neurosurgical intervention was performed: mass removal for 6 lesions and Ommaya reservoir placement for the other 8. Among these 12 patients, 6 with neurologic symptoms experienced complete recovery. Although no neurologic symptoms had developed, surgical intervention was performed for the other 7 because sequential MRI follow-up had demonstrated progressive enlargement of a cyst and/or a mass lesion, and further observation had thus been regarded as constituting an excessively high risk. During the median postsurgical interval of 25 months (range, 2-80 months), the 12 patients experienced no further exacerbation until death or the latest follow-up day. Among 8 patients who had undergone Ommaya reservoir placement, repeated aspiration with a 1-3-month interval was required in 2, and no further aspiration was necessary in the other 6.

### Factors affecting delayed complications

As shown in Tables 1 and 3, among various pre-GKRS clinical factors, univariate analysis demonstrated tumor volume-related factors: largest tumor volume (HR, 1.091; 95% CI, 1.018-1.154;  $P=.0174$ ) and tumor volume  $\leq 10$  cc vs  $>10$  cc (HR, 4.343; 95% CI, 1.444-12.14;  $P=.0108$ ) to be the only significant predictors of delayed complications. Univariate analysis revealed no correlations between delayed complications and radiosurgical parameters (ie, radiosurgical doses, conformity and gradient indexes, and brain volumes receiving  $>5$  Gy and  $>12$  Gy) (9-12). After GKRS, an area of prolonged enhancement at the irradiated lesion on MRI performed at the 12th post-treatment month or later was shown to be a possible risk factor for delayed complications (HR, 8.751; 95% CI, 1.785-157.9;  $P=.0037$ ).

### Neuroimaging and pathology

Among the 17 patients who experienced delayed complications, a progressively expanding mass lesion developed in 8. Sequential MRI studies, methionine PET scans or proton MR spectrograms, and histologic findings in these 8 patients are shown in Figs. 2 and 3. Histologic examinations were not available in 2 patients (patients 2 and 5) because they refused surgery. However, high methionine uptake was not demonstrated on PET scans in patient 2, and a higher choline peak was not seen on the proton MR spectrogram in patient 5. Therefore, we considered recurrence to be unlikely in these mass lesions. Histologic studies were performed in the other 6 patients, and no tumor cells were found. Characteristic histologic features were hypocellular scar tissue consisting of fibrous tissue with degenerative cells, sinusoid

**Table 3** Clinical factors affecting incidence of delayed complications (167 patients)

Clinical factors	Univariate analysis		
	HR	95% CI	P values
Age			
Continuous	1.010	0.977-1.051	.5730
<65 vs $\geq 65$ y	0.949	0.324-2.523	.9192
Sex: female vs male	1.073	0.402-2.812	.8851
KPS: $\geq 80\%$ vs $\leq 70\%$	5.192	0.278-28.52	.2067
Primary cancer: lung vs nonlung	0.398	0.124-1.098	.0761
Prior surgery: no vs yes	0.474	0.109-1.457	.2072
Prior WBRT: no vs yes	0.908	0.049-4.797	.9265
GKRS procedures			
Continuous	1.153	0.820-1.524	.3830
Single vs multiple	1.155	0.424-3.225	.7775
Tumor numbers			
Continuous	1.066	0.968-1.131	.1567
Solitary vs multiple	0.699	0.266-1.841	.4710
Tumor volume			
Cumulative	1.090	1.022-1.151	.0117
Largest tumor*	1.091	1.018-1.154	.0174
$\leq 10$ cc vs $>10$ cc	4.343	1.444-12.14	.0108
Tumor nature			
Solid vs cystic	1.057	0.335-4.644	.9313
Peritumoral edema: yes vs no	1.589	0.574-4.167	.3586
Accompanying hemorrhage: yes vs no	NA	NA	.1783
Area of prolonged enhancement: yes vs no <sup>†</sup>	8.751	1.785-157.9	.0037
Dose			
Minimum	1.008	0.905-1.147	.8977
Maximum	1.025	0.961-1.096	.4517
Conformity index <sup>‡</sup>	10.33	0.355-378.4	.1765
Gradient index <sup>‡</sup>	1.427	0.601-3.125	.4186
Brain volume receiving $>5$ Gy <sup>†</sup>	1.000	0.994-1.003	.8558
Brain volume receiving $>12$ Gy <sup>†</sup>	1.005	0.983-1.021	.5915

Abbreviations: CI = confidence interval; GKRS = Gamma Knife radiosurgery; HR = hazard ratio; KPS = Karnofsky performance status; NA = not available; WBRT = whole brain radiation therapy.

\* Tumors causing delayed complications in the complication (+) group and the largest tumors in the complication (-) group.

<sup>†</sup> Demonstrated on magnetic resonance imaging (MRI) performed at the 12th post-treatment month or later (16 patients were excluded because MRI results were not available).

<sup>‡</sup> Based on 162 patients (5 were excluded because treatment data were lost owing to technical problems).

formation, variously sized vessels, endothelial proliferation, various stages of hemorrhage, and hemosiderin deposits.

### Discussion

Historically, the purpose of treating patients with brain metastases has been symptom palliation and maintenance of good condition during the patient's relatively short remaining life expectancy.

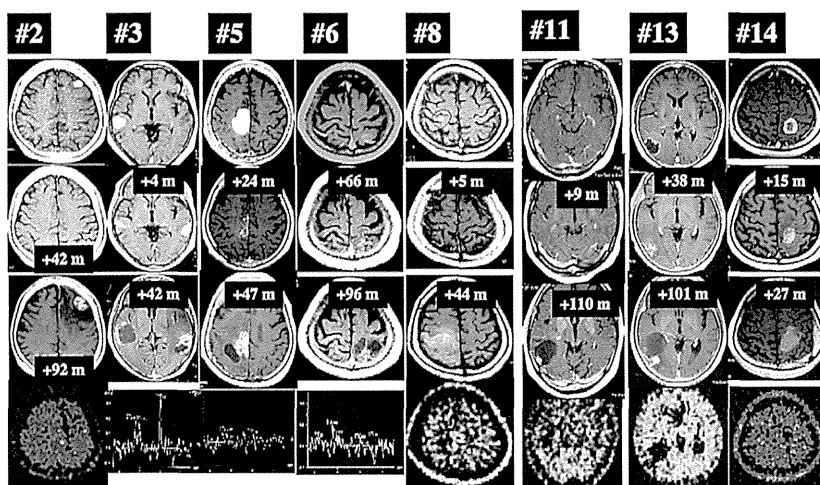


**Fig. 2.** Sequential magnetic resonance (MR) images, methionine positron emission tomographic (PET) scans, or proton MR spectrograms of 8 patients. Patient numbers are shown above each column. MRI was performed at the time of Gamma Knife radiosurgery (GKRS) (*top row*), at the time of confirmed tumor control (at the time of the second GKRS for a left temporal tumor in patient 3) (*second row*), and at the time of the development of delayed complications (*third row*). Methionine PET scans or proton MR spectrograms were obtained at nearly the same times as the upper MR examinations (*bottom row*).

Therefore, treatment-related complications occurring with a long latency period have seldom been a matter of primary concern. However, SRS, which is a less invasive procedure and allows long-term tumor control, has recently become a common treatment for brain metastases (1, 2). As we have reported elsewhere, GKRS was shown to benefit patients by decreasing the likelihood of death from neurologic causes (approximately 10%) (8, 13). The widespread use of SRS for patients with brain metastases has recently prompted physicians to continue, rather than give up, as in the former era, aggressive treatment of original tumors and/or extracranial metastases. With recent advances in cancer treatment, considerable numbers of patients can survive for many years after the initial diagnosis. This has raised concern regarding post-SRS complications occurring with a prolonged latency period. Very recently, learning how to avoid and treat these complications has

been seen as crucial. To the best of our knowledge, this retrospective investigation is the first to analyze the long-term toxicity of SRS in patients surviving at least 3 years after treatment of brain metastases.

### Incidences of complications

Williams et al (14) recently reported the incidences of post-SRS complications and their predictive factors based on a comprehensive review of 273 patients (316 treated lesions) undergoing SRS for 1 or 2 brain metastases. According to their investigation, complications, mostly seizure onset, were associated with 127 (40%) of 316 treated lesions. Severe complications were more likely to occur more than 30 days after SRS. Progression of the

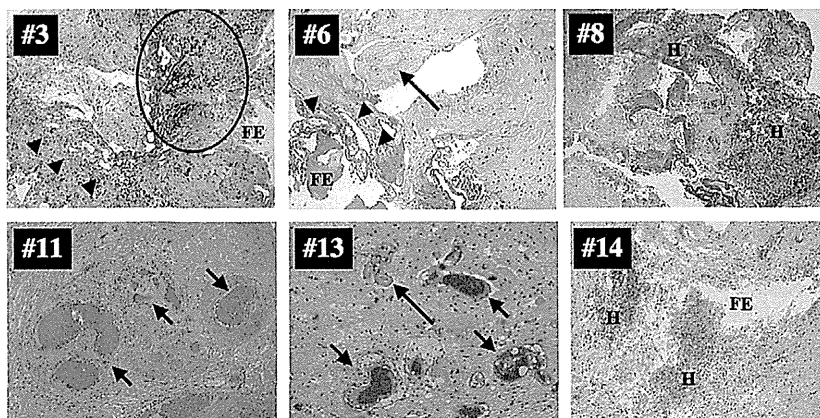


**Fig. 3.** Histopathologic findings in 6 patients. Excluding 1 deceased patient (patient 8), the remaining 5 agreed to the use of their histopathologic photographs for this publication. Patient numbers are shown in each image. Notice various sized vessels (*short arrows*), endothelial proliferation (*long arrows*), sinusoid formation (*arrowhead*), fluid exudation (*FE*), various stages of hemorrhage (*H*), and hemosiderin deposits (*circle*). (Hematoxylin and eosin, original magnifications not available.)



primary cancer and tumor location in the eloquent cortex were significantly associated with complications. However, no chronologic data were presented in their article, and there was no description of delayed complications. Varlotto et al reported (11) that among 137 patients with brain metastases who survived for at least 1 year after GKRS, postradiosurgical sequelae developed in 2.8% and 11.4% of patients at the first and fifth year, respectively, after GKRS. The incidence of 11.4% at the fifth post-GKRS year was far higher than our result, 4.2%. In their study, only the standard Kaplan-Meier method was used. This method assumes that follow-up of those developing a competing event (death) is simply censored. We consider competing risk analysis to have been necessary for evaluation of their data (6, 7). Furthermore, their Kaplan-Meier plot of the proportion without neurologic sequelae showed that none of their patients experienced neurologic sequelae between the 24th and 120th post-GKRS months. In other words, Varlotto et al (11) observed complications that occurred in a somewhat earlier post-GKRS period, 2 years or less. By contrast, herein we have described delayed complications occurring 24 months or more after GKRS, and our data demonstrated a time-related increase in the incidence (Fig. 1).

### Predictive factors

Several authors have shown correlations with tumor volume and/or WBRT and complications (11, 14-17). In our present study, the only factor associated with delayed complications was larger tumor volume. Nakagawa et al reported prior or concomitant WBRT to be a possible risk factor for low-grade dementia (16). We also observed 1 patient in whom severe dementia occurred after WBTR followed by GKRS (8). However, in our series, a small number of patients—only 4—underwent WBRT, so the correlation between WBRT and delayed complications was unclear. It is common knowledge in radiobiology that higher irradiation doses carry a higher risk of complications. The median peripheral dose, 24.0 Gy, in the subset reported here was higher than the 21.0 Gy in our entire cohort (2000 cases). We cannot deny that such a relatively high dose may have an impact on delayed complications, although univariate analysis did not demonstrate the peripheral dose to be a predictive factor for delayed complications in this study (Table 3).

Paddick and Lippitz (10) found, among several radiosurgical parameters, the gradient index to be a crucial factor for complication avoidance. Also, Ishikawa et al (3) described, as noted in our previous report on delayed cyst formation after GKRS for patients with brain metastases, that a poor gradient index may partially explain the observed phenomenon. However, univariate analysis did not demonstrate the gradient index to be a predictive factor for delayed complications in this study. Although Varlotto et al (11) found that complications correlated with brain volume receiving  $\geq 12$  Gy and we reported receiving  $\geq 5$  Gy to be important (12), neither  $\geq 12$  Gy nor  $\geq 5$  Gy irradiated brain volume was associated with delayed complications in our present study.

### Pathogenesis

The first author (M.Y.) previously reported post-GKRS sequelae (ie, expanding mass lesions with or without cyst formation) occurring many years after GKRS for arteriovenous malformations (18, 19). Our present study revealed similar complications to occur in long-term survivors after GKRS for brain metastases. As noted in our

previous report, the mechanism of delayed cyst formation after GKRS for brain metastases is speculated to be increased permeability through partially injured blood vessel walls within the degenerated or scar tissue (3). However, the mechanism of enhanced mass lesions has yet to be fully elucidated. The histopathologic changes of resected specimens in the 6 cases reported herein were characterized as degenerated tissue mainly consisting of fibrous tissue and various stages of hemorrhage, from fresh to organized with hemosiderin deposits. Also, there was evidence of neovascularization, enlarged vessels, and albuminous fluid exudation. In most cases, the irradiated metastatic lesions showed findings from coagulation necrosis to liquefaction necrosis and ultimately collapsed, as Szeifert et al very recently described (20). However, we speculate that in some other cases, degenerated tissue remains for many years and reparative processes may occur after repeated intranidal microhemorrhage, which may finally cause an expanding mass lesion, although the triggering mechanism remains unknown. Therefore, the existence of a long-standing enhanced area may be a risk factor for delayed complications.

### Treatment

Observation alone is reasonable for compensated and asymptomatic patients because spontaneous regression can be expected in some, as is the case in patients with arteriovenous malformations. When delayed cysts and/or enhanced mass lesions are symptomatic, surgical intervention should be considered. Even if these conditions have not yet produced neurologic symptoms, surgical intervention is recommended for patients whose cysts and/or mass lesions show continuous expansion. For a patient with a simple cyst, we believe that Ommaya reservoir placement may be a better choice than fluid aspiration without a reservoir, because some patients require reaspiration. Moreover, Ommaya tube placement may maintain the drainage tract from the cyst to the subarachnoid space, thereby preventing cyst regrowth. For a patient with an enhanced mass lesion with or without cyst formation, however, surgical resection should be considered even if the mass lesion is not particularly large. In any case, the surgical results of our present series were favorable.

### Conclusions

In conclusion, 10.2% of long-surviving patients showed delayed complications, with a median interval of 53 months (range, 24.0-121.0 months) after GKRS for brain metastases. A larger tumor volume, particularly larger than 10 cc, was a risk factor for these complications. Long-term follow-up is crucial for patients with brain metastases treated with GKRS because the risk of complications long after treatment is not insignificant. However, if a delayed complication does occur, a favorable outcome can be expected with timely surgical intervention. This is considered to be quite different from WBRT, which causes the untreatable complication of decreased NCF.

### References

1. Linskey ME, Andrews DW, Asher AL, et al. The role of stereotactic radiosurgery in the management of patients with newly diagnosed brain metastases: a systematic review and evidence-based clinical practice guideline. *J Neurooncol* 2010;96:45-68.

2. McDermott MW, Sneed PK. Radiosurgery in metastatic brain cancer. *Neurosurgery* 2005;57(Suppl S4):45-53.
3. Ishikawa E, Yamamoto M, Saito A, et al. Delayed cyst formation after gamma knife radiosurgery for brain metastases. *Neurosurgery* 2009; 65:689-695.
4. Radiation Therapy Oncology Group Cooperative Group Common Toxicity Criteria. <http://www.rtog.org/ResearchAssociates/AdverseEventReporting.aspx>. Accessed September 30, 2011.
5. Gasper L, Scott C, Rotman M, et al. Recursive partitioning analysis (RPA) of prognostic factors in three Radiation Therapy Oncology Group (RTOG) brain metastases trials. *Int J Radiat Oncol Biol Phys* 1997;37:745-751.
6. Gooley TA, Leisenring W, Crowley J, et al. Estimation of failure probabilities in the presence of competing risks: new representations of old estimators. *Stat Med* 1999;18:695-706.
7. Fine JP, Gray RJ. A proportional hazards model for the subdistribution of a competing risk. *J Am Stat Assoc* 1999;94:496-509.
8. Yamamoto M. Radiosurgery for metastatic brain tumors. *Prog Neurol Surg* 2007;20:106-128.
9. Paddick I. A simple scoring ratio to index the conformity of radio-surgical treatment plans. *J Neurosurg* 2000;93(Suppl):219-222.
10. Paddick I, Lippitz B. A simple dose gradient measurement tool to complement the conformity index. *J Neurosurg* 2006;105(Suppl): 194-201.
11. Varlotto JM, Flickinger JC, Niranjan A, et al. Analysis of tumor control and toxicity in patients who have survived at least one year after radiosurgery for brain metastases. *Int J Radiat Oncol Biol Phys* 2003;57:452-464.
12. Yamamoto M, Ide M, Nishio S, et al. Gamma knife radiosurgery for numerous brain metastases: is this a safe treatment? *Int J Radiat Oncol Biol Phys* 2002;53:1279-1283.
13. Yamamoto M, Kawabe T, Bierta E, et al. How many metastases can be treated with radiosurgery? *Prog Neurol Surg* 2012;26: 261-272.
14. Williams BJ, Suki D, Fox BD, et al. Stereotactic radiosurgery for metastatic brain tumors: a comprehensive review of complications. *J Neurosurg* 2009;111:439-448.
15. Joseph J, Adler JR, Cox RS, et al. Linear accelerator-based stereotaxic radiosurgery for brain metastases: the influence of number of lesions on survival. *J Clin Oncol* 1996;14:1085-1092.
16. Nakagawa K, Tago M, Terahara A, et al. A single institutional outcome analysis of gamma knife radiosurgery for single or multiple brain metastases. *Clin Neurol Neurosurg* 2000;102:227-232.
17. Shiau CY, Sneed PK, Shu H, et al. Radiosurgery for brain metastases: relationship of dose and pattern of enhancement to local control. *Int J Radiat Oncol Biol* 1997;37:375-383.
18. Yamamoto M, Jimbo M, Hara M, et al. Gamma knife radiosurgery for arteriovenous malformations: long-term follow-up results focusing on complications occurring more than five years after irradiation. *Neurosurgery* 1996;38:906-914.
19. Yamamoto M, Hara M, Ide M, et al. Radiation-related adverse effects observed on neuro-imaging several years after radiosurgery for cerebral arteriovenous malformations. *Surg Neurol* 1998;49: 387-398.
20. Szeifert GT, Kondziolka D, Lunsford LD, et al. The contribution of pathology to radiosurgery. *Prog Neurol Surg* 2007;20:1-15.

## Analysis of progression and recurrence of meningioma using $^{11}\text{C}$ -methionine PET

Hidetoshi Ikeda · Naohiro Tsuyuguchi ·  
Noritsugu Kunihiro · Kenichi Ishibashi ·  
Takeo Goto · Kenji Ohata

Received: 31 January 2013 / Accepted: 16 June 2013 / Published online: 26 June 2013  
© The Japanese Society of Nuclear Medicine 2013

### Abstract

**Objective** The recurrence rate of meningioma after surgery is high, and progression is often observed. The risk factors for recurrence and progression are not clear. We evaluated the risk factors for recurrence and progression in meningioma using  $^{11}\text{C}$ -methionine (MET) positron emission tomography (PET).

**Methods** Thirty-seven patients (mean follow-up, 80 months) with an intracranial meningioma were enrolled. MET PET was performed before treatment between 1995 and 2010, and patients were followed up in an out-patient clinic. Surgery was performed in 33 patients, and a wait-and-see approach was taken in four patients. We evaluated the extent of tumor resection, location, WHO grade, Ki-67 labeling index, and lesion to normal ratio (LN ratio) of MET uptake.

**Results** Six of the surgical cases had a recurrence, and two of the observation-only patients had tumor progression. A high LN ratio of MET uptake was a significant risk factor for recurrence and progression with univariate analysis. The area under the curve of receiver operating characteristic curve for the LN ratio of MET uptake was 0.754, and the optimal cutoff value was 3.18 (sensitivity 63 %, specificity 79 %). With multivariate analysis, a high LN ratio of MET uptake, non-gross total resection, and a high WHO grade were significant risk factors for progression and recurrence.

**Conclusion** A high LN ratio of MET uptake was a risk factor for tumor progression and recurrence. The advantage of MET PET is that it is not invasive and can easily be used to evaluate the whole tumor.

**Keywords**  $^{11}\text{C}$ -methionine PET · Meningioma · Riskfactor of recurrence and progression · Multivariable analysis · ROC analysis

### Introduction

Meningioma is the most common primary brain tumor in adults. The frequency of meningioma among all types of brain tumors is 26.4 % in Japan [1] and 34.4 % in the United States. Many histopathological subtypes exist. Most meningiomas are benign, but World Health Organization (WHO) grade II and grade III meningiomas, which exhibit aggressive clinical behavior, are found in 10 % of patients with meningioma. We usually perform surgery for symptomatic cases or cases with large tumors. For small and asymptomatic cases, a wait-and-see approach is taken. However, gross total resection (GTR) is difficult in some surgical cases because of the tumor location and invasion into the brain tissue and the venous sinus. The residual tumor often recurs with malignancy, making the patient's prognosis poor. Meningiomas that are only observed sometimes progress and require surgical resection. In previous papers, the recurrence rate after surgery was high. Even if the tumor is removed completely, the recurrence rate is between 7 and 32 %. After subtotal resection, the recurrence rate is between 19 and 50 % [2–4].

The risk factors for progression and recurrence in meningioma are not clear, and clarification of these factors is important for determining surgical indications and

H. Ikeda (✉) · N. Tsuyuguchi · N. Kunihiro · K. Ishibashi ·  
T. Goto · K. Ohata  
Department of Neurosurgery, Osaka City University Graduate  
School of Medicine, 1-4-3 Asahi-machi, Abeno-ku,  
Osaka 545-8585, Japan  
e-mail: hide-i@med.osaka-cu.ac.jp

treatment strategies. We usually use the Ki-67 labeling index (LI) to evaluate the proliferative activity, but surgery is required to obtain a tissue specimen. Surgery is invasive for the patient, and evaluating the risk of recurrence with the Ki-67 LI is controversial because the tissue specimen sometimes does not reflect the whole tumor.

In this study, we evaluated  $^{11}\text{C}$ -methionine (MET) uptake of the whole tumor using MET positron emission tomography (PET) to investigate the risk factors for recurrence and progression.

## Methods

### Patients

From a database of patients who were examined with MET PET, we retrospectively retrieved data for all 73 patients who were diagnosed with intracranial meningioma between 1995 and 2010. These cases were not a consecutive series. We could not examine MET PET results for all meningioma cases because the number of cases that could be examined by MET PET per week in our facilities is limited. Thirty-seven patients fulfilled the inclusion criteria for this study: (1) patients were initially diagnosed with meningioma; (2) MET PET was performed before surgery or observation; (3) patients were followed at Osaka City University Hospital or affiliated hospitals; (4) during the follow-up period, no additional treatment was performed other than the first surgery. Thirty-three patients were excluded because of recurrence after surgery, and three patients dropped out during the follow-up period. Thus, 37 cases (23 females and 14 males) were enrolled in this study (Fig. 1). The mean age of the patients was  $54.5 \pm 12.9$  years. All study participants provided

informed consent, and the study design was approved by an ethics review board.

### MET PET study

All patients underwent a MET PET scan with HEADTOME-IV (BGO, Shimadzu, Japan) between 1995 and 2005, Eminence-B (BGO) since 2005, and Biograph-16 (LSO, Siemens, Germany) since 2010. Twenty-six patients were examined with HEADTOME-IV. Axial and in-plane resolutions of the PET images were each 4.5 mm (in full width at half maximum), and the slice thickness was 4 mm. Twenty minutes after MET injection (4 MBq/kg), an emission scan of the brain was performed for 10 min. The emission scan was reconstructed to a matrix of  $128 \times 128$  (using an iterative algorithm), and attenuation and scatter correction were done. The voxel size was  $2 \times 2 \times 3.25$  mm.

Ten patients were examined with Eminence-B. Axial and transaxial resolutions of the PET were each 4.5 mm (in full width at half maximum). The injection volume and timing of the scan were the same as HEADTOME-IV. The emission scan was reconstructed to a matrix of  $128 \times 128$ , and attenuation and scatter correction were done. The voxel size was  $2 \times 2 \times 3.25$  mm.

One patient was examined with Biograph-16. Axial and transaxial resolutions of the PET were 5.5 and 5.9 mm (in full width at half maximum), respectively. The injection volume and timing of the scan were the same as HEADTOME-IV. The emission scan was reconstructed to a matrix of  $336 \times 336$ , and attenuation and scatter correction were done. The voxel size was  $1.02 \times 1.02 \times 2$  mm.

All MET PET images were interpreted by an experienced neurosurgeon. The MET uptake was calculated by drawing a region of interest (ROI) using a freehand procedure. In all cases, MET uptake of the lesion was higher than in normal gray matter. In cases with a multiple meningioma, the lesion with the highest mass was evaluated. From the tumor lesion and normal reference region (frontal lobe of the normal side), the lesion to normal ratio (LN ratio) of mean MET uptake was calculated.

### Surgical resection, pathological findings, and clinical follow-up

Thirty-three cases were treated with surgery, and four cases were observed. In surgical cases, GTR (Simpson grade I or II) was performed in 18 cases (55%), and subtotal resection (Simpson grade III or IV) was performed in 13 cases (39%). Partial resection (Simpson grade IV) was performed in one case (3%), and a biopsy (Simpson grade V) was performed in one case (3%). The pathological diagnosis and the WHO grade were determined by experienced

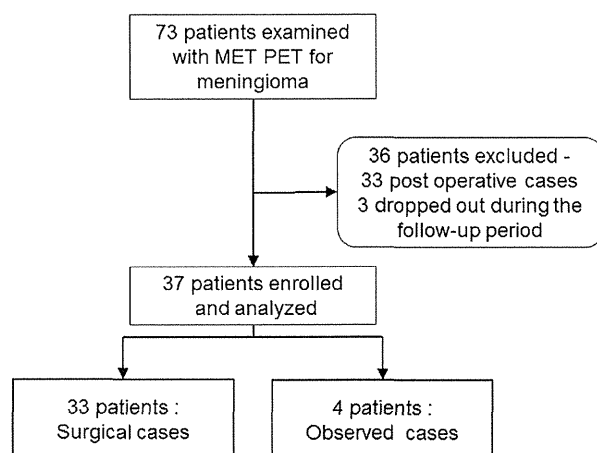


**Fig. 1** Analysis of meningioma cases with MET PET